coatings

MDPI

Article

Corrosion Mechanisms of a Biodegradable Zn-0.4Li Alloy in Simulated Gastrointestinal Environment

Manli Wang [1,2], Lingbo Yang [1], Xinglong Zhu [1], Lijing Yang [1,*], Jianwei Shen [3], Ting Lu [3], Huinan Liu [4] and Zhenlun Song [1]

[1] Key Laboratory of Marine Materials and Related Technologies, Zhejiang Key Laboratory of Marine Materials and Protective Technologies, Ningbo Institute of Materials Technology and Engineering, Chinese Academy of Sciences, Ningbo 315201, China
[2] University of Chinese Academy of Sciences, Beijing 100049, China
[3] Ningbo Medical Center Lihuili Hospital, Ningbo 315041, China
[4] Department of Bioengineering, University of California, Riverside, CA 92521, USA
* Correspondence: yanglj@nimte.ac.cn

Abstract: Zn-Li alloys have been demonstrated to be potential biodegradable materials because of their favorable biocompatibility and exceptional strength. The corrosion behaviors of Zn–0.4Li in simulated gastric fluid (SGF) and simulated intestinal fluid (SIF) were investigated. Compared with samples in SIF, those in SGF were severely corroded locally. Pepsin and pancreatin participated in the formation of degradation products. After immersion in SGF and SIF, the corrosion process presented two interfaces. Lithium (Li) preferentially reacted in the near-surface region to form a Li-rich region. Simultaneously, there were two Li-poor regions around the Li-rich region. Then Zn-rich products gradually became dominant with time. Li^+ releasement dominated over Zn^{2+} releasement throughout the immersion process in SGF and SIF. These results can guide the development of biodegradable gastrointestinal anastomotic nails in the future.

Keywords: zinc; gastrointestinal environment; corrosion mechanism

check for updates

Citation: Wang, M.; Yang, L.; Zhu, X.; Yang, L.; Shen, J.; Lu, T.; Liu, H.; Song, Z. Corrosion Mechanisms of a Biodegradable Zn-0.4Li Alloy in Simulated Gastrointestinal Environment. *Coatings* **2023**, *13*, 529. https://doi.org/10.3390/coatings13030529

Academic Editor: Alina Vladescu

Received: 24 December 2022
Revised: 13 February 2023
Accepted: 24 February 2023
Published: 28 February 2023

Copyright: © 2023 by the authors. Licensee MDPI, Basel, Switzerland. This article is an open access article distributed under the terms and conditions of the Creative Commons Attribution (CC BY) license (https://creativecommons.org/licenses/by/4.0/).

1. Introduction

Gastrointestinal cancer has become one of the cancers with the highest morbidity and mortality. When removing a diseased intestinal tract, mechanical anastomosis is employed to reconstruct the continuity of the intestinal tract. In gastroenterostomy, surgical staples are widely used instead of traditional sutures for the healing and reconstruction of the gastrointestinal tract to greatly improve the surgical efficiency, reduce postoperative complications and relieve patients' pain [1]. Most suture nails at present are made of titanium (Ti) alloy; they are not degradable and may cause adverse reactions, such as allergic reaction, foreign body reaction and tissue adhesion in the body [2,3]. Given the high X-ray absorption coefficient of Ti, metal artifacts may be produced during computed tomography, and these may interfere with the postoperative examination of patients and result in misdiagnosis.

Zinc (Zn) alloys, as new candidate materials for biodegradable metals, have attracted much attention due to their moderate degradation rate, outstanding mechanical properties and benign biocompatibility [4–8]. Studies on Zn alloys have achieved progress in various areas, such as vascular stents and orthopedics [5,9–13]. Guo et al. studied the residual stress and biocompatibility of Zn–Mn–Li anastomotic nails in simulated gastric fluid (SGF) immersion [14]. Guo et al. investigated the mechanical mismatch of Zn–0.1Li in simulated intestinal fluid (SIF) [9]. But there is still no clear understanding of how Zn alloys degrade in the digestive tract environment, although such a mechanism is crucial for the development, design and application of degradable Zn alloy nails in the future. The mouth, pharynx, esophagus, stomach, small intestine, and large intestine make up the

majority of the digestive tract. These components play different roles in digestion, and their internal environments differ [15–17]. The stomach is primarily used to grind large pieces of food into small pieces and break down the large molecules in the food into small ones for further absorption. Therefore, hydrochloric acid, Cl^-, mucus, sodium salt, pepsin, and other substances are primarily found in gastric juice with a pH value of 1–3 [16]. After the initial digestion and decomposition of food in the stomach, it enters the small intestine, which is the main place for the human body to digest food and absorb nutrients. The intestinal fluid contains many pancreatic enzymes and buffers to neutralize gastric acid and shield the intestinal membrane from acid damage. The pH value in the small intestine ranges within 5.0–7.7 [17,18]. The difference between the stomach and intestinal environment exerts different effects on the degradation of Zn alloys.

The mechanical characteristics of biodegradable metal scaffolds need to meet the following criteria in order to be used in clinical settings: yield strength (YS) > 200 MPa, ultimate tensile strength (UTS) > 300 MPa, and elongation at break (EL) > 15%–18% [18]. According to previous studies [19–27], among binary Zn alloys, only Zn-Mg [23] alloys and Zn-0.8Li alloy [27] can surpass the standard in certain circumstances. Moreover, Zn–Li alloy has superior strength among all binary Zn alloys and has an appropriate degradation rate and satisfactory biocompatibility [5,28,29]. In addition, 1.0 mg of Li per day is recommended for an American adult weighing 70 kg in order to meet their daily requirement, which can be met by diet [30]. For more than 50 years, Li has been the first-line treatment for bipolar disorder. Li may have cardioprotective effects in addition to its neuroprotective effects, according to recent clinical and laboratory investigations [31]. Mazor et al. discovered that Li had a particular tumor-inhibiting impact [32]. However, there are some potential health hazards associated with consuming excessive amounts of Li. Li is not harmful in the therapeutic range of 0.6 to 1.0 mM, but toxicity levels start to appear at 1.4 mM or higher, according to clinical experience [33]. Zn levels in human serum should range between 12.4–17.4 μmol/L. Zn is a trace element that is vital for the body's immune system and bone growth [34]. However, neurotoxicity issues may result from excessive Zn [35]. Studies conducted in vivo and in vitro by Yang et al. revealed that the effect of Zn–0.4Li alloy on cell proliferation and osteogenic activity was much superior to that of pure Zn. Therefore, in this study, immersion experimentation and electrochemical testing were used to identify the mechanism of extruded Zn–0.4Li degradation in intestinal and gastric environments with significant pH differences. The degradation mechanism of Zn alloy in simulated digestive tract environments was revealed, providing reference for the development of degradable Zn alloy nails and digestive tract stents in the future.

2. Materials and Methods

2.1. Alloy Preparation

The alloy in this study was prepared by Ningbo Powerway Alloy Material (Ningbo, China) Co., LTD. The ingots were annealed at 260 °C for 2.5 h. The annealed ingots were then extruded at 220 °C with a 20:1 extrusion ratio. The diameter of the extruded alloy bars was 11 mm. The actual chemical composition of the nominal alloy of Zn–0.4Li (wt%) was measured to be Zn–0.373Li (wt%) via inductively coupled plasma optical emission spectrometry (ICP/OES). The Zn/Li ratio in Zn-0.4Li was 26.8. The metals were cut into a size of φ11 mm × 2 mm. All samples were ground with P2000 grit SiC sandpaper separately and then cleaned in distilled water and absolute ethanol for 5 min in turn.

2.2. Immersion Tests

According to ASTM G31-72, immersion tests were carried out for 1, 3, and 7 days in SGF and SIF at a temperature of 37 °C and an immersion ratio of 0.05 cm^2/mL. Chinese Pharmacopoeia Iv contains information on the precise methods for making SGF and SIF. SGF was composed of 10 g/L of porcine pepsin and 16.4 mL/L of dilute hydrochloric acid with the pH adjusted to 1.2. SIF was composed of 10 g/L of porcine pancreatin, 6.8 g/L of KH_2PO_4 and 0.1 mol/L of NaOH with the pH adjusted to 6.8. KH_2PO_4 (AR), HCl (AR) and

NaOH (AR) were purchased from Sinopharm Chemical Reagent Co. Ltd. Pepsin (1:3000) and pancreatin (1:250) were purchased from Shanghai Macklin Biochemical Technology Co., Ltd.

The tubes and specimens were sterilized with ultraviolet light to avoid bacterial and fungal growth, and liquid penicillin-streptomycin was injected into SGF/SIF at a ratio of 1:100. Five samples were prepared in parallel for each experiment. The staples were taken out at various immersion durations, then dried in a vacuum furnace for 1 h at 100 °C. In order to eliminate the degradation products from the samples, they were submerged in 200 g/L of Cr_2O_3 at 40 °C for 5 min. The mass loss method was then used to calculate the degradation rates. The corrosion rate was calculated as follows [36]:

$$CR = \frac{K\Delta m}{\rho A t} \quad (1)$$

where CR is the corrosion rate in mm/year, the coefficient $K = 8.76 \times 10^4$, Δm is the mass loss in g, ρ is the density of the material in g/cm^2, A is the initial surface area in cm^2 and t is the immersion time in h.

2.3. Microstructure Observation and Corrosion Product Analysis

The microstructure of the material was observed through scanning electron microscopy (SEM; FEI Quanta FEG 250, Hillsboro, OR, USA) before and after immersion. The samples were immersed and analyzed utilizing X-ray diffraction (XRD; Bruker D8 ADVANCE, Karlsruhe, Germany) with Cu Kα radiation between the 2θ values of 10° and 90° to determine the composition of the samples and degradation products. An X-ray photoelectron spectrometer (XPS; Axis Ultra DLD, Shimadzu, Kyoto, Japan) was used to analyze the composition of the corrosion products. To understand the corrosion mechanism, ICP/OES was employed to detect the element concentration in the immersion solution at different times. The extent to which the samples were corroded by the solution was determined through glow discharge-optical emission spectroscopy (GD-OES; GDA, Spectruma 750HP, Frankfurt, Germany) with minimum resolution depth of 25 nm.

2.4. Electrochemical Measurements

Electrochemical tests were performed on the Zn–0.4Li alloys in SGF and SIF with an M237A electrochemical workstation (Princeton M273A). A typical three-electrode cell was employed; the specimen served as the working electrode, a platinum-sheet acted as the counter electrode, and the saturated calomel electrode worked as the reference electrode. The sample, which was encased in the resin, had a surface area of 0.95 cm^2 to touch the electrolyte. Data on open-circuit potential (OCP) were gathered for a maximum of 7 days. With a potential fluctuation range of ±10 mV, electrochemical impedance spectroscopy (EIS) was carried out in the frequency band from 100 kHz to 10 MHz. The potentiodynamic polarization (PDP) curves were obtained in a range of ±2 V vs. OCP at a constant scan rate of 0.5 mV·s^{-1}. Additionally, samples were submerged in solutions for 30 min to allow OCP to stabilize before the test. Three replications of each test were run in order to confirm the consistency of the outcomes.

3. Results

3.1. Microstructure Characterization

Figure 1a shows that the extruded Zn–0.4Li alloys were mainly composed of Zn and $LiZn_4$ phases. Figure 1b presents the microstructures of the Zn–0.4Li alloys. The composition of Zn-0.4Li was near the eutectic point of 0.44% Li. According to the equilibrium phase diagram of Zn-Li [22,37], the eutectic structure of Zn + $LiZn_4$ is developed after the main Zn phase is first established. The replacement of Zn atoms with Li atoms made the standard electrode potential (E°) of Zn highly negative due to the E° of Li (i.e., −3.04 V) being much lower than that of Zn (i.e., −0.76 V). Thus, $LiZn_4$ particles were more vulnerable to the corrosion, resulting in a recessed topography and a darker color [27,38,39]. Zn phase should

be used in regions that are brighter and more resistant to corrosion. The eutectic phase (Zn + $LiZn_4$), in contrast, should be the darker region with more severe etching properties, as indicated by the yellow arrows in the high-magnification SEM image (Figure 1c).

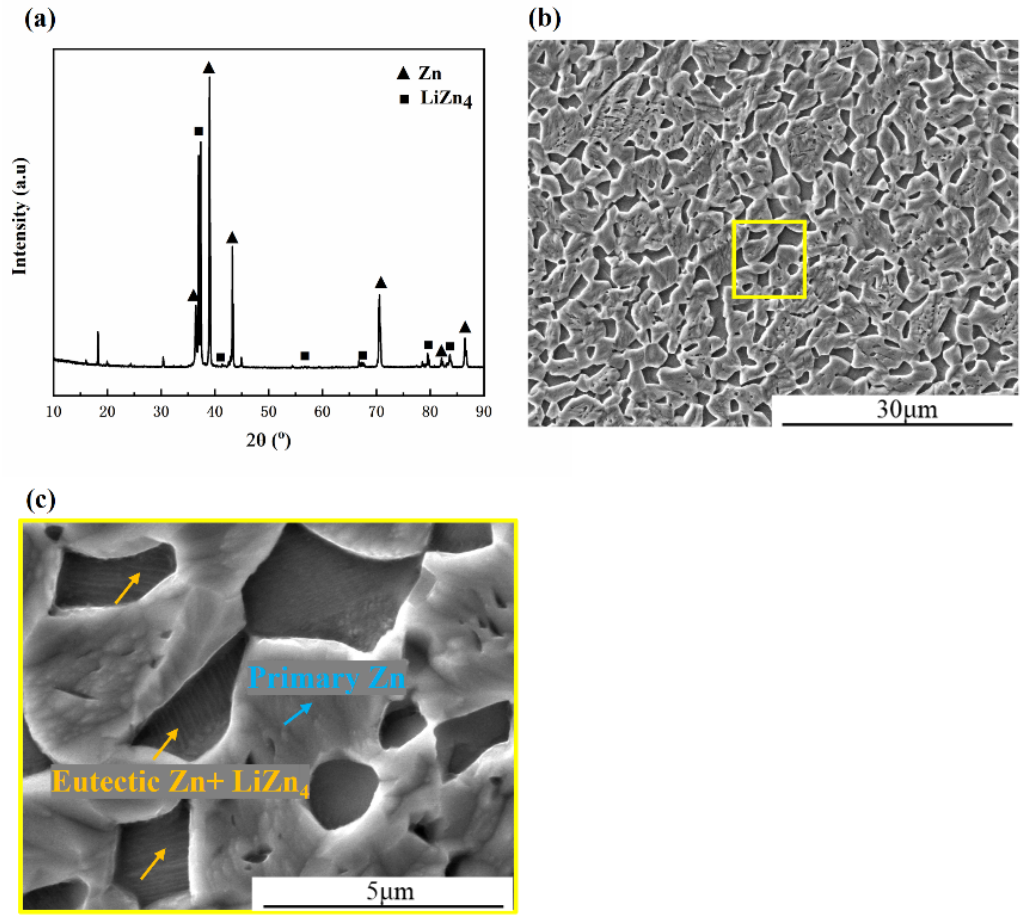

Figure 1. Microstructure characterization of Zn–0.4Li before immersion in solutions. (**a**) XRD spectra and (**b**) SEM image. (**c**) High-magnification image of the yellow frame.

3.2. Immersion Test

Figure 2 presents the corresponding corrosion rates and pH of samples immersed in SGF and SIF at different times. The corrosion rate in SGF was much higher than that in SIF. The corrosion rate of the sample in all of the solutions reached the maximum value at the initial stage of immersion and then decreased with the increase in time. Guo et al. also observed the same phenomenon [9]. The phenomenon suggests the formation of a corrosion product layer on the surface of the sample. The SIF's pH was determined to be reasonably stable, with changes not exceeding 0.1. The samples were extensively corroded, and a significant number of alkaline compounds were released into the SGF under the overall influence of a substantial amount of H^+ and Cl^- in the solution. (In the Section 4, the specific content was explained.) The large amounts of H^+ ions were consumed at the same time, causing a significant shift in the pH value of SGF, which rose with time.

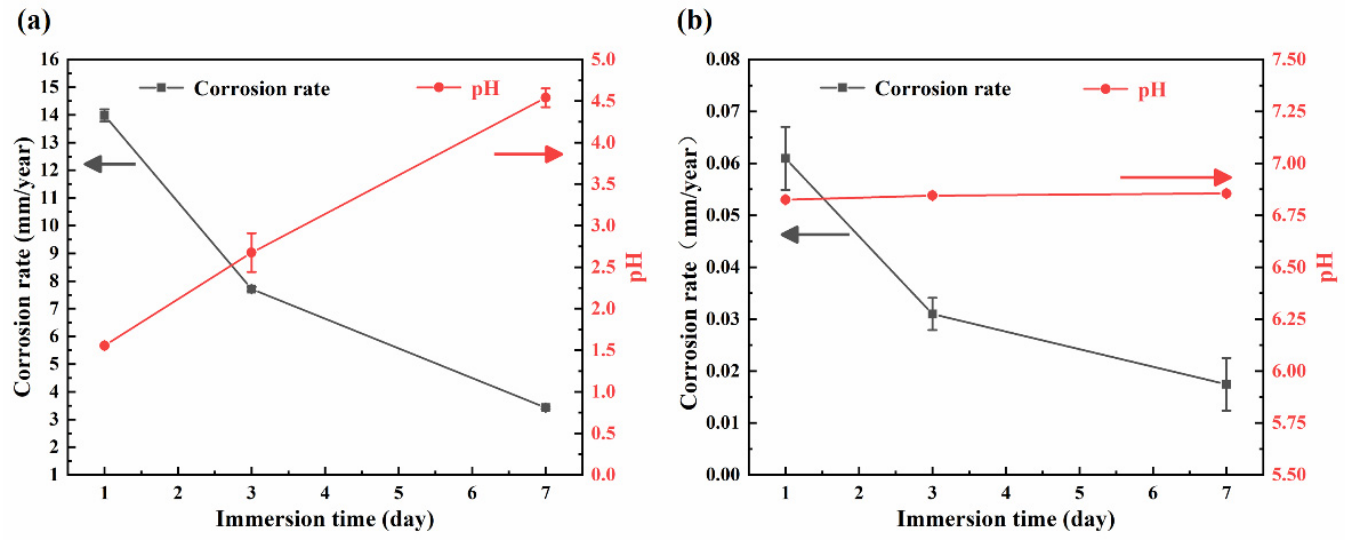

Figure 2. Corrosion rate and pH of Zn–0.4Li immersed in SGF and SIF at different times: (**a**) in SGF and (**b**) in SIF.

3.3. Surface Morphology and Chemical Composition

The phase compositions of the corrosion products (on the alloy surface) in SGF and SIF are shown in Figures 3 and 4. The SEM morphologies of the corrosion products formed on the Zn–0.4Li surfaces during immersion in SGF and SIF for 1, 3 and 7 days are displayed in Figure 3a. No obvious difference was observed in the morphologies of Zn–0.4Li after immersion in SIF at different times (Figure 3a). The sample immersed in SIF mainly exhibited uniform corrosion. After immersion in SIF, a layer of the corrosion products with dark micropores covered the sample surface, as indicated by the high-magnification area in Figure 3a. The density and depth of the micropores varied with immersion time. Notably, round flower-like corrosion products occupied most of the sample surface after immersion in SIF for 3 days, as shown in Figure 3a. These round flower-like corrosion products were formed because the sample surfaces absorbed abundant PO_4^{3-} in the solution during immersion in SIF [40].

Figure 3b presents SEM images of Zn–0.4Li after the removal of the corrosion products. The morphologies of the samples immersed in SIF showed little difference between the samples with and without the corrosion products removed, possibly due to the short immersion time and minimal accumulation of corrosion products. According to Figure 3a,b, after immersion in SGF, the surface of the sample was covered with multitudes of dark-grey corrosion pits, and large-diameter corrosion pits appeared in local areas, indicating intensive localized corrosion. The longer the immersion time was, the more obvious the non-uniform corrosion was. The number and depth of corrosion pits increased with time. After immersion for 7 days, the maximum diameter of the corrosion pits exceeded 150 μm. In the SGF, the severe pits and localized corrosion of Zn–0.4Li were due to the attack ion of Cl^-. The localized corrosion due to galvanic corrosion resulted from segregation of the secondary $LiZn_4$ phase on grain boundaries for Zn–0.4Li alloy [39]. As we knew, the phase boundaries were the interface of galvanic coupling for the dual-phase zinc alloys. The corrosive Cl^- preferentially attacked at the interface of the $LiZn_4$ phase and Zn phase. Then, the localized corrosion initiated from the phase boundaries [41].

The main phase compositions of the corrosion products of the samples after 7 days of immersion in SGF and SIF were analyzed through XRD, as shown in Figure 3c. Figure 3c suggests that the main phase compositions of the corrosion products in SIF included $Zn_5(CO_3)_2(OH)_6$, ZnO, $Zn_3(PO_4)_2{\bullet}4H_2O$ and Li_2CO_3. Figure 3c reveals that the corrosion products in SGF included $Zn_5(CO_3)_2(OH)_6$, ZnO and Li_2CO_3. Notably, $Zn(OH)_2$ was not detected probably because of its unstable properties and rapid regeneration to ZnO [42].

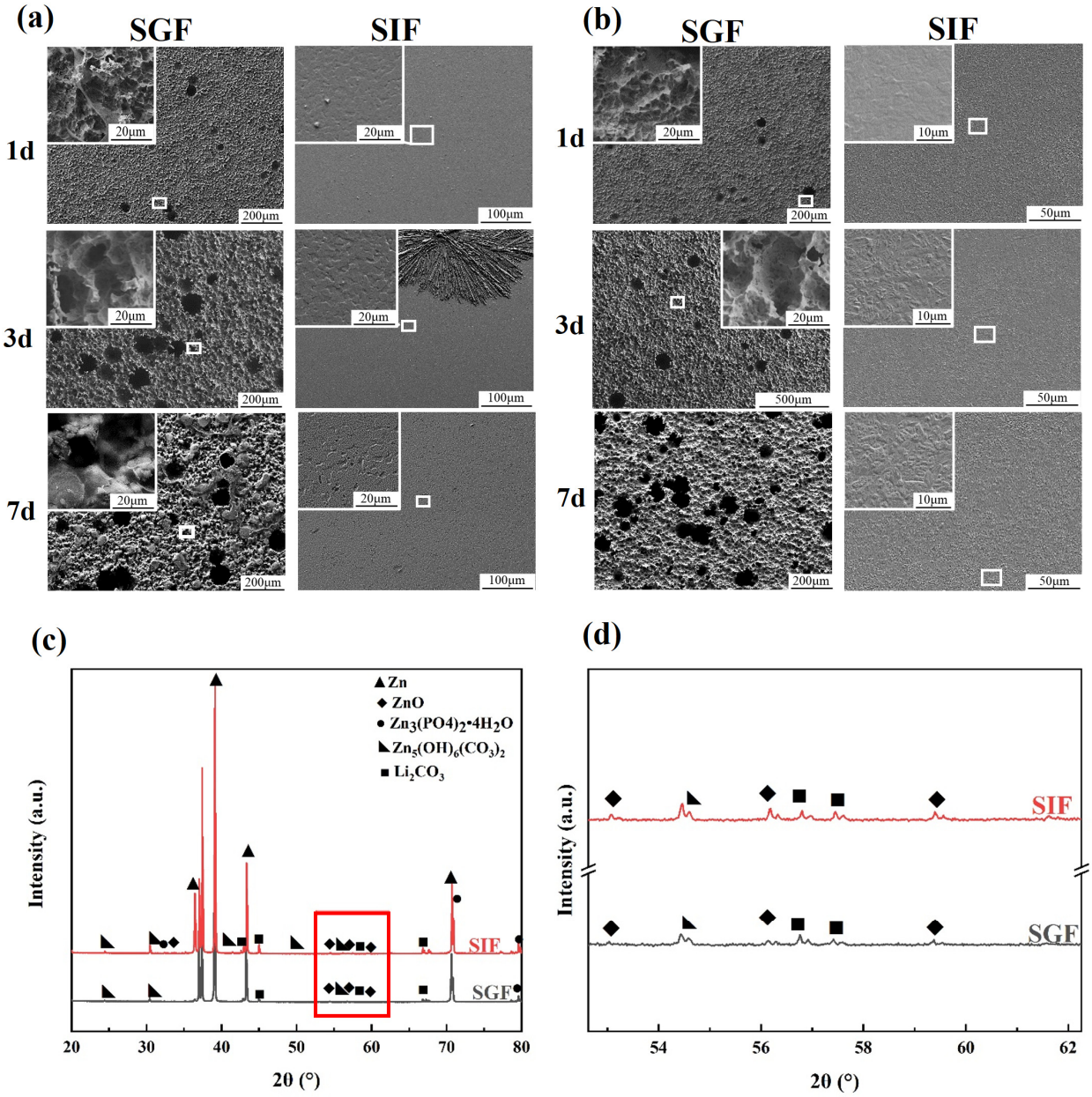

Figure 3. In vitro degradation behaviors of Zn–0.4Li alloy in SGF and SIF. (**a**) SEM images of Zn–0.4Li immersed in SGF and SIF at different time, and (**b**) surface morphologies after the removal of corrosion products. The areas enclosed by white squares are observed at high magnification. (**c**) XRD analysis of degradation products. (**d**) Enlarged image of the red frame.

Figure 4 displays the XPS results, which served as supplements to further analyze the phase composition of the corrosion products in SGF and SIF. The peaks for Zn 2p, O 1s, N 1s and C 1s were detected on the sample surface in SGF after 1 and 7 days of immersion, as shown in Figure 4a. The peak for P 2p was also detected in SIF (Figure 4a). As depicted in Figure 4b, for SGF, within 1 day, Li was abundant (i.e., roughly 27.6 at%) and Zn was minor (i.e., <5.1 at%) in the corrosion products. They then underwent opposite trends of change. Zn rose to 16.6 at% on day 7, while Li fell to 0 at%. These trends signified the transformation from Li-rich corrosion products to Zn-rich corrosion products [38,39,43]. However, Li was not found in the XPS spectrum of samples immersed in SIF. These indicate that the SGF and SIF corroded the $LiZn_4$ phase in the surface layer more than other phases [43]. The existence

of the N element proved that enzymes played a role in the development of products on the sample surfaces.

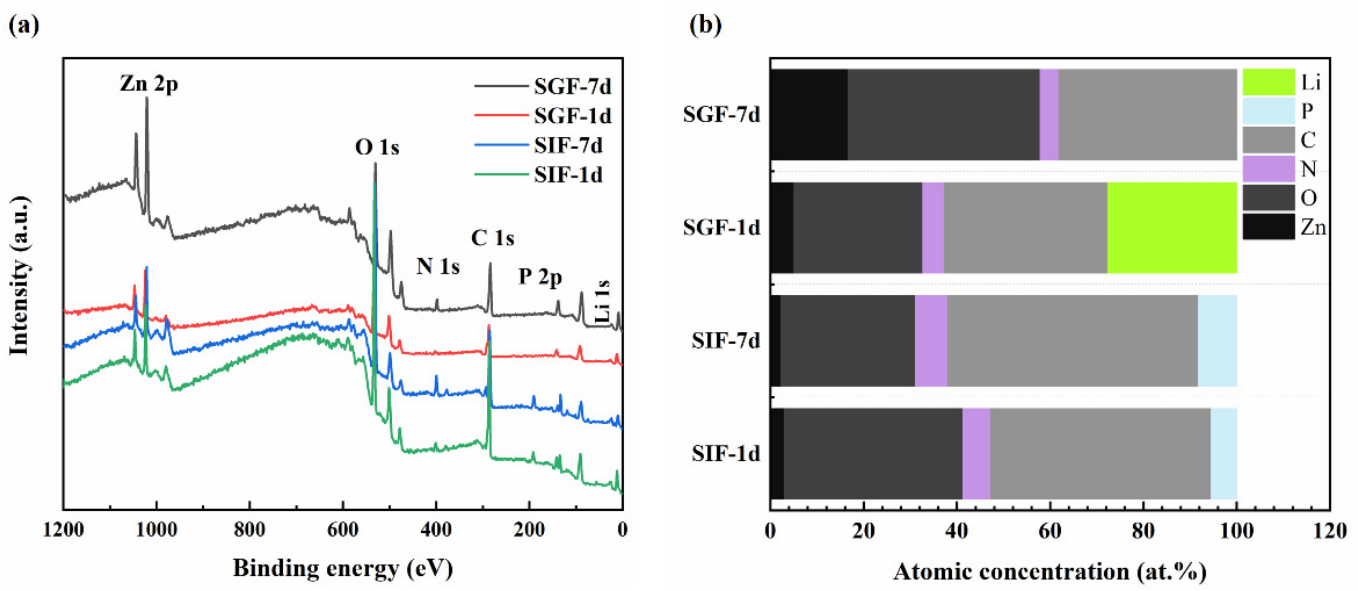

Figure 4. Immersion in SGF and SIF for 1 and 7 days: (**a**) XPS spectra; (**b**) atomic concentration of elements detected by XPS.

Additionally, Figure 5(a–c,a1–c1) shows the high-resolution XPS spectra of Zn 2p, C 1s, and N 1s for Zn-0.4 Li alloys following 7 days of immersion in SGF and SIF. In Table 1, the binding energies of the various substances taken into consideration for XPS spectral analysis are provided. The Zn 2p spectra are depicted in Figure 5(a,a1). ZnO and $Zn_5(CO_3)_2(OH)_6$ were the dominant corrosion products within 7 days in SGF. We also found $Zn_3(PO_4)_2 \bullet 4H_2O$ in SIF. Figure 5(b,b1) shows the fitting curves of the C 1s spectra of the corrosion products of the samples after immersion for 7 days in SGF and SIF, respectively. The peaks at 7 days showed good fitting with five contributions at 284.5, 285.4, 286.2, 287.5 and 288.3 eV. The peak at 284.5 eV was ascribed to the C-H/C-C bond, and the high binding-energy signals were separately ascribed to C-N, C-O, C=O and O=C-N. The peak at 286.2 eV was attributed to the protein backbone's NH-CHR-CO carbons, and the peak at 288.3 eV was attributed to the protein's -CO-NH- peptide bond [44,45]. The C-N and C=O-NH bonds that came from the amine or amide groups in enzymes supplied two components at 399.4 and 400.0 eV, respectively, according to the deconvolution of the N 1s spectra (Figure 5(c,c1)) [46,47]. These characteristic bands illustrated the presence of enzymes on the surfaces of the samples after immersion [48].

Table 1. Binding energy and corresponding compounds in the XPS spectra of Zn–0.4Li surfaces after immersion for 7 days.

Element	Characterized Bonds	Binding Energy (eV)	References
Zn 2p	ZnO	1022	[49]
	$Zn_5(CO_3)_2(OH)_6$	1022.3	[49]
	$Zn_3(PO_4)_2 \bullet 4H_2O$	1022.5	[49]
C 1s	C-H/C-C	284.5	[44,45]
	C-N	285.4	[44,45]
	C-O	286.2	[44,45]
	C=O	287.5	[44,45]
	O=C-N	288.3	[44,45]
N 1s	C-N	399.4	[46,47]
	C=O-NH	400.0	[46,47]

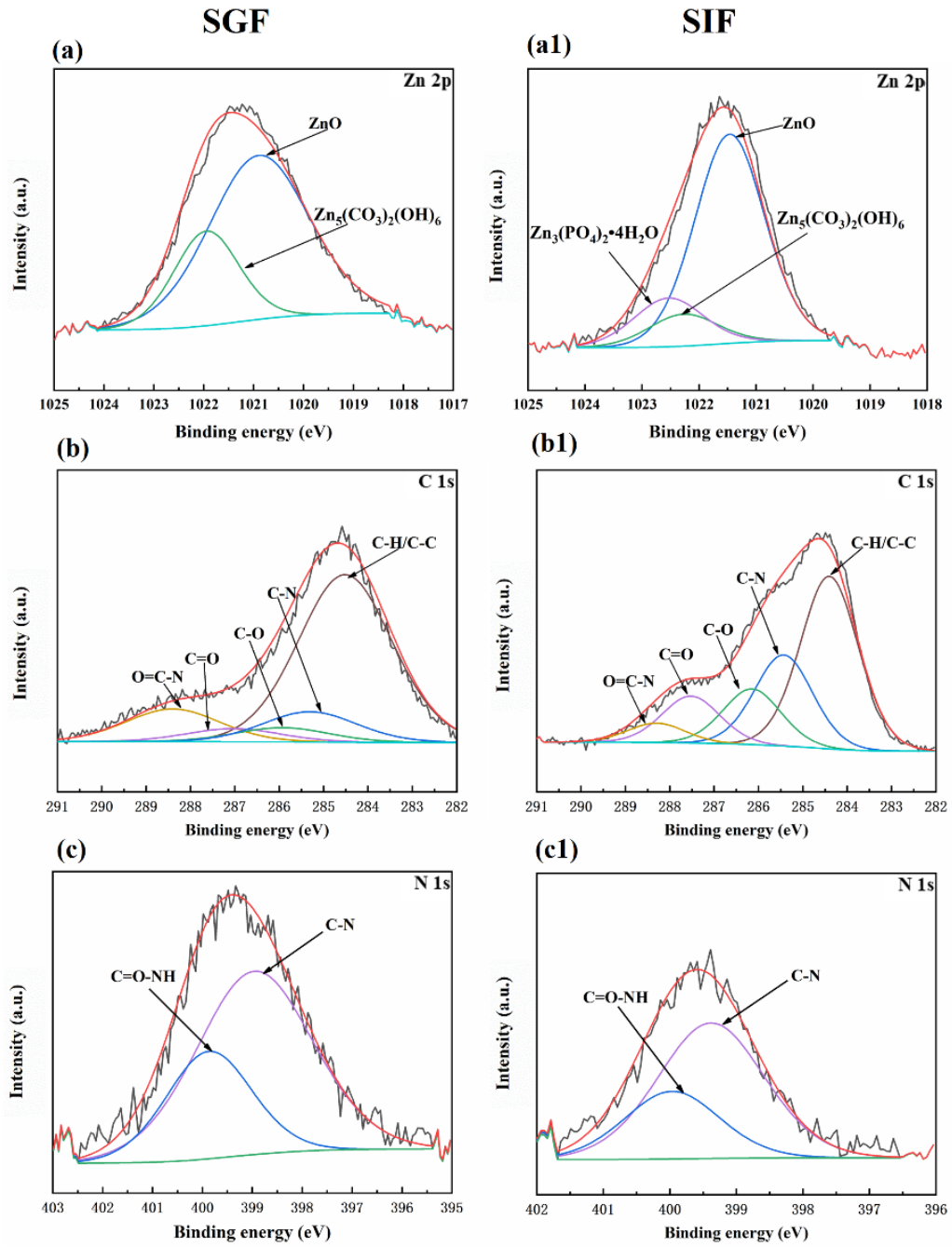

Figure 5. XPS spectrum of the samples immersed in SGF and SIF for 7 days. (**a**–**c**) Zn–0.4Li alloy in SGF; (**a1**–**c1**) in SIF. (**a**,**a1**) Zn 2p, (**b**,**b1**) C 1s and (**c**,**c1**) N 1s.

XPS is a non-destructive measurement technology that detects material surface information through a photon beam incident onto the sample surface at a depth of 3–10 nm. The thin films formed on the samples in SGF/SIF in this study were analyzed via GD-OES, as shown in Figure 6. Almost no Li element was detected within 0.5 µm from the surfaces of the samples after 7 days of immersion in SGF/SIF (Figure 6c,d). As a result, Li was not detected in XPS spectra for samples immersed 7 days (Figure 4).

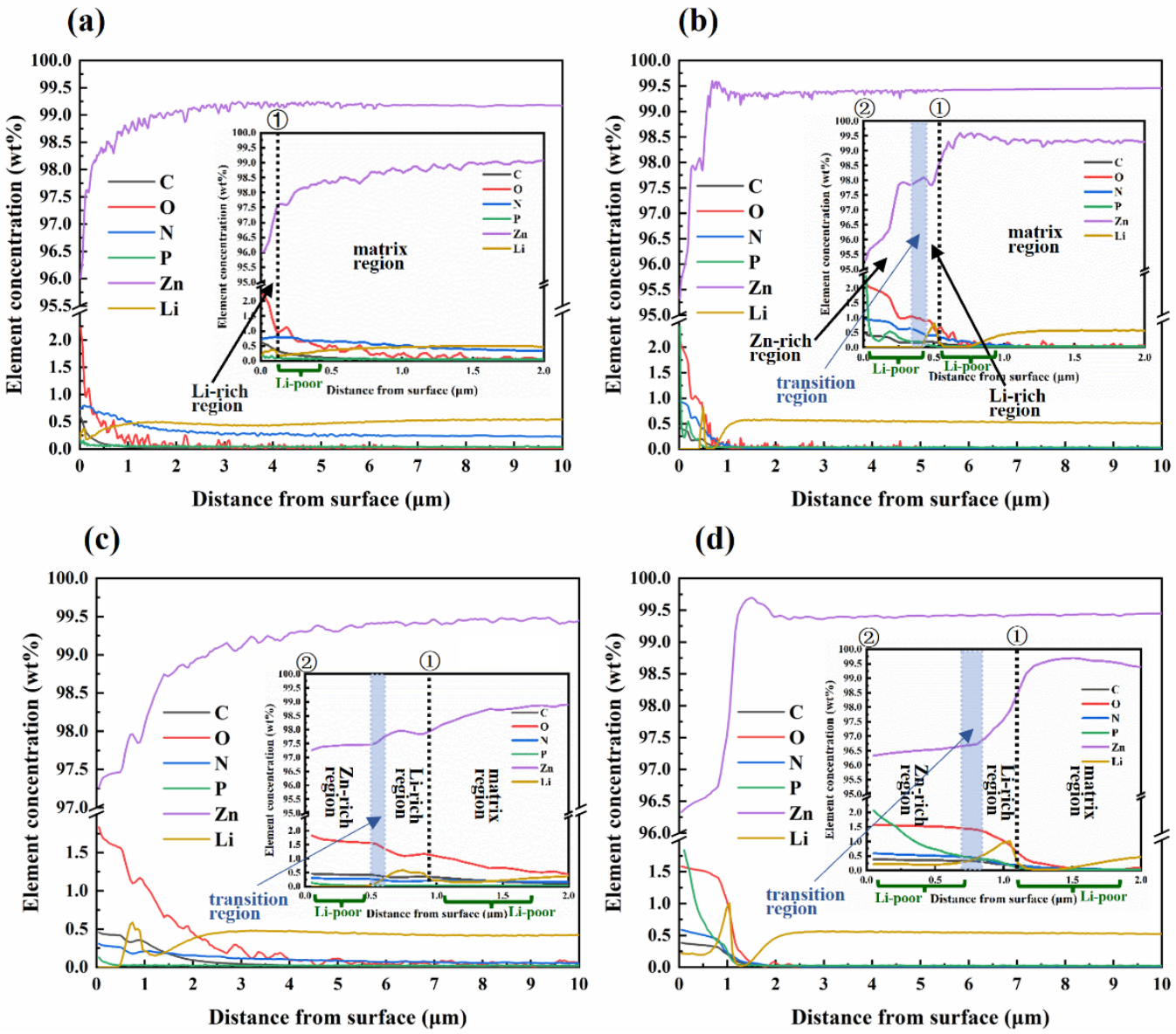

Figure 6. GD-OES depth profiles of Zn–0.4Li immersed in SGF (**a**,**c**) and SIF (**b**,**d**). (**a**,**b**) For 1 day, (**c**,**d**) for 7 days. ①: interface 1, ②: interface 2. The insert is an enlarged view from the surface of the sample to 2 μm inside.

Figure 6a,c demonstrates the distribution of elements along the depth of the sample immersed in SGF for 1 and 7 days, respectively. The insert (Figure 6a) was divided into Li-rich and matrix regions based on the reaction of Li and Zn element. The reactions of interfaces 1 and 2 are discussed in detail in the Section 4. The results of immersing in SGF for 1 day were consistent with the results of XPS (Figure 4b), indicating that the corrosion products on the surface contained considerable amounts of Li-rich products. At day 7, the weight percentage (wt%) of Li was approximately 0 wt% within 0.5 μm of the sample surface (Figure 6c). On the other hand, Zn exhibited a different pattern, rising from 96 wt% on day 1 to 97.25 wt% on day 7. A similar phenomenon was also found from the elemental analysis (Figure 4b). The insert for immersion 7 days in SGF was divided into Zn-rich region, transition region, Li-rich region and matrix region. Li-poor and Li-rich regions can be seen in Figure 6a,c. Figure 6b shows the concentration of each element with the distance from the sample surface after immersion in SIF for 1 day. At 0.5 μm from the surface, a Li-rich region was observed in the sample immersed in SIF for 1 day. The Li-rich

region moved to 1 μm away from the surface after immersion for 7 days (Figure 6d). In the Li-rich region, the content of Zn increased sharply. At about 0.25 μm, the content of N decreased rapidly, indicating that pancreatin was involved in the formation of corrosion products on the first day (Figure 6b). Additionally, two Li-poor regions were also observed around the Li-rich region. The reason for the formation of the Li-poor region near the sample surface above the Li-rich region after immersion in SGF is that the region is in direct contact with the solution, and Li is directly corroded and dissolved into the solution [38,39]. Li ions quickly emerge from the matrix and gather close to the surface. Then Li^+ ions react with CO_3^{2-} primarily to produce substantial quantities of Li_2CO_3(Figure 3b) and deposit to form Li-rich region. The Li-poor region of the substrate beneath the Li-rich region was due to Li atoms in the deeper part of the matrix that could not diffuse to the surface in time. These reasons also apply to the phenomenon of Li-rich and Li-poor regions in the samples in SIF. Subsequently, when near-surface regions became Li-poor regions, the reaction between Zn and H_2O became dominant and resulted in the formation of ZnO and $Zn_5(CO_3)_2(OH)_6$ (Figures 3c and 5a), resulting in the dominant Zn-rich products in the later stages of immersion. With the prolongation of immersion time, the corrosion of Li ions on the surface of the sample worsened, and the Li-poor region expanded to the interior of the sample, making the Li-rich area migrate to the interior of the sample. The range of the Li-rich region widened at 7 days due to the accumulation of Li ions. The total eroded depth after immersion for 7 days in the GD-OES experiments was about 1.9 μm in SIF and 2.7 μm in SGF. The range of Zn-rich and Li-rich regions grew with the lengthening of immersion time, indicating the buildup of corrosion products on the samples' surfaces, as found by comparing the depth profiles of GD-OES samples immersed in SGF and SIF for 1 and 7 days.

Compared with the situation in SGF, the Li-rich and Zn-rich regions of the samples immersed in SIF for 1 day were wider. In addition, the diagram of the element distribution on the surfaces of the samples immersed for 1 and 7 days shows an obvious stage of sudden decrease in O element in SIF, but this stage was not observed in the whole process of SGF immersion. No effective oxidation layer was formed on the surface of the sample immersed in SGF with a low pH value, and most of the corrosion products dissolved into the solution.

3.4. Competitive Mechanisms of Zn and Li in the Degradation Process

The Zn/Li ratio in Zn-0.4Li was 26.8. The Li^+/Zn^{2+} atomic ratio was more than 75 in all of the solutions during immersion (Figure 7a,b), demonstrating that Li^+ releasement dominated over Zn^{2+} releasement in the anode corrosion reaction [39,50]. Li was actively corroded. In SGF, the Li^+/Zn^{2+} atomic ratio decreased in the first 3 days and then increased gradually. This phenomenon also appeared in the samples immersed in SIF. Initially, the Li atoms in the surface layer were preferentially corroded and dissolved into the solution, and this can be seen in Figure 6a. When Li was consumed, Zn began to corrode, thus reducing the Li^+/Zn^{2+} atomic ratio. As shown in Figure 6c,d, the Li-rich region, where O, C and Li ions together formed a compact oxide layer, widened after immersion for 7 days. Owing to the compact oxide layer accumulation preventing further corrosion of Zn, the Li^+/Zn^{2+} atomic ratio increased in the late period of immersion. Notably, the Li^+/Zn^{2+} atomic ratio in SIF was always higher than that in SGF. The samples immersed in SGF corroded at a greater rate than the samples immersed in SIF (Figure 2). Compared with the degradation rate of Li atoms, the degradation rate of Zn in the samples immersed in SIF was much lower than that in SGF. Obviously, strong acid and plentiful Cl^- in the SGF environment made it clearly distinct from SIF. Cl^- ions have the potential to cause localized corrosion and the disruption of passive films [51,52]. A low pH value is not conducive to passivation film formation. On the other hand, the corrosion rate can be slowed down by the passivation film that is created by hydrogen phosphate and Zn ions [40,49,53]. Owing to these factors, the corrosion of Zn atoms in the sample proceeded slowly in SIF in the current study. Zhang et al. [54] found that pancreatin and pepsin have different effects

on preventing metal corrosion, but their effects on Zn degradation remain to be studied further.

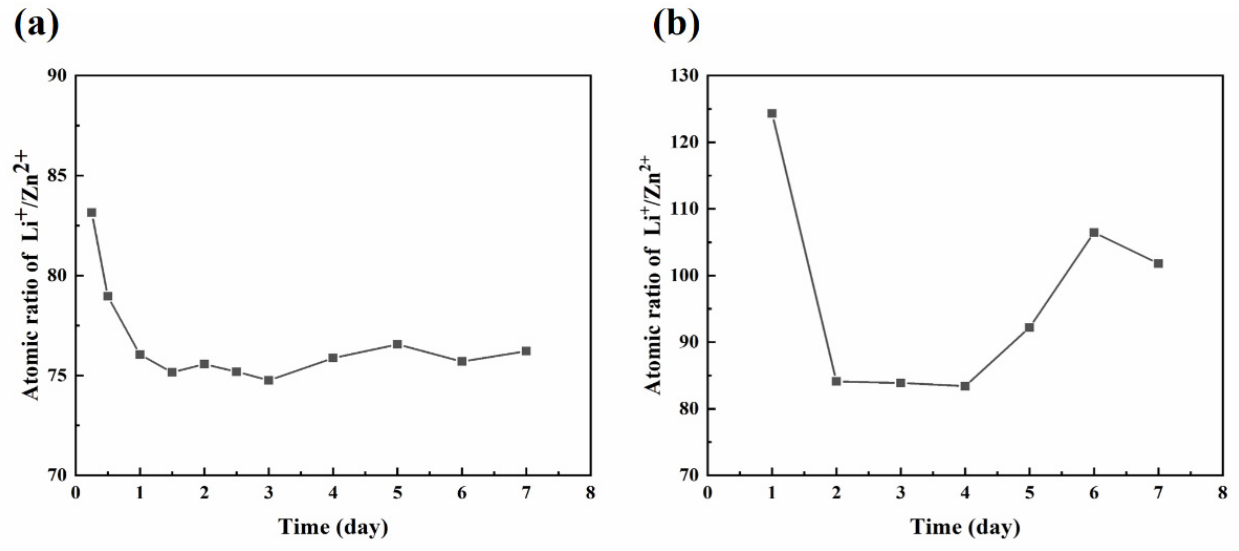

Figure 7. Releasing Li^+/Zn^{2+} atomic ratio in SGF (**a**) and SIF (**b**) at different times.

3.5. Electrochemical Characterization

Figure 8a,b shows the anodic and cathodic PDP curves of Zn–0.4Li at different times in SGF and SIF. Figure 8c,d provides a list of the relative electrochemical corrosion parameters that were identified by PDP. The values of corrosion potential (E_{corr}) and corrosion current density (i_{corr}) of the sample soaked in SIF were calculated using Tafel extrapolation of the cathodic region, while E_{corr} and i_{corr} of the sample soaked in SGF were obtained using the Tafel extrapolation method with both the anodic and cathodic Tafel regions [55–57]. i_{corr} is a kinetic parameter used to assess the rate of corrosion. In this study, on the first day, the i_{corr} value increased compared with that on day zero and then decreased with immersion time in SGF (Figure 8c), which corresponded with the corrosion rate obtained using the mass loss approach (Figure 2a). When the samples were immersed in SGF, E_{corr} changed very little with time. With the exception of a minor fluctuation, the E_{corr} of the samples immersed in SIF drifted towards positive values with duration. This finding showed a decreased sensitivity of the sample to corrosion. For the anodic branch, a passive region appeared in the samples in SIF, indicating that a film provisionally formed on the surface and impeded corrosion, whereas the Zn–0.4Li alloy in SGF was corroded continuously. Moreover, the range of the passive region of SIF increased with the extension of immersion time, revealing a high kinetic barrier effect on anodic dissolution with immersion time. The corrosion pattern discovered by the electrochemical test was similar to the corrosion trend discovered by the immersing experiment.

The curves in Figure 9 represent the variation of the OCP values of the Zn–0.4Li electrode with time in SGF and SIF. The value of OCP was more negative in SIF than in SGF. For SIF, the corrosion potentials shifted from approximately −1.1 V and increased quickly during the first 0.5 days, with fluctuations in the range of approximately 10%. This behavior might be connected to the collaborative activity of oxides and enzymes on the sample surfaces during immersion [58]. Then, some sharp drops in corrosion potentials were observed from the first 0.5 day to 1 day. After the first day, the corrosion potentials remained stable with a low fluctuation frequency until 2.5 days. The OCP of SIF changed periodically within a period of about 2.5 days; this may have resulted from the adsorption and subsequent desorption of enzymes or the shedding of corrosion products during immersion [48]. For SGF, OCP shifted cathodically with small fluctuations. The phenomenon in SGF was mainly due to the pH value of the solution being 1.2, and the amount of H^+ in the solution was presumably too large to form an effective protective film.

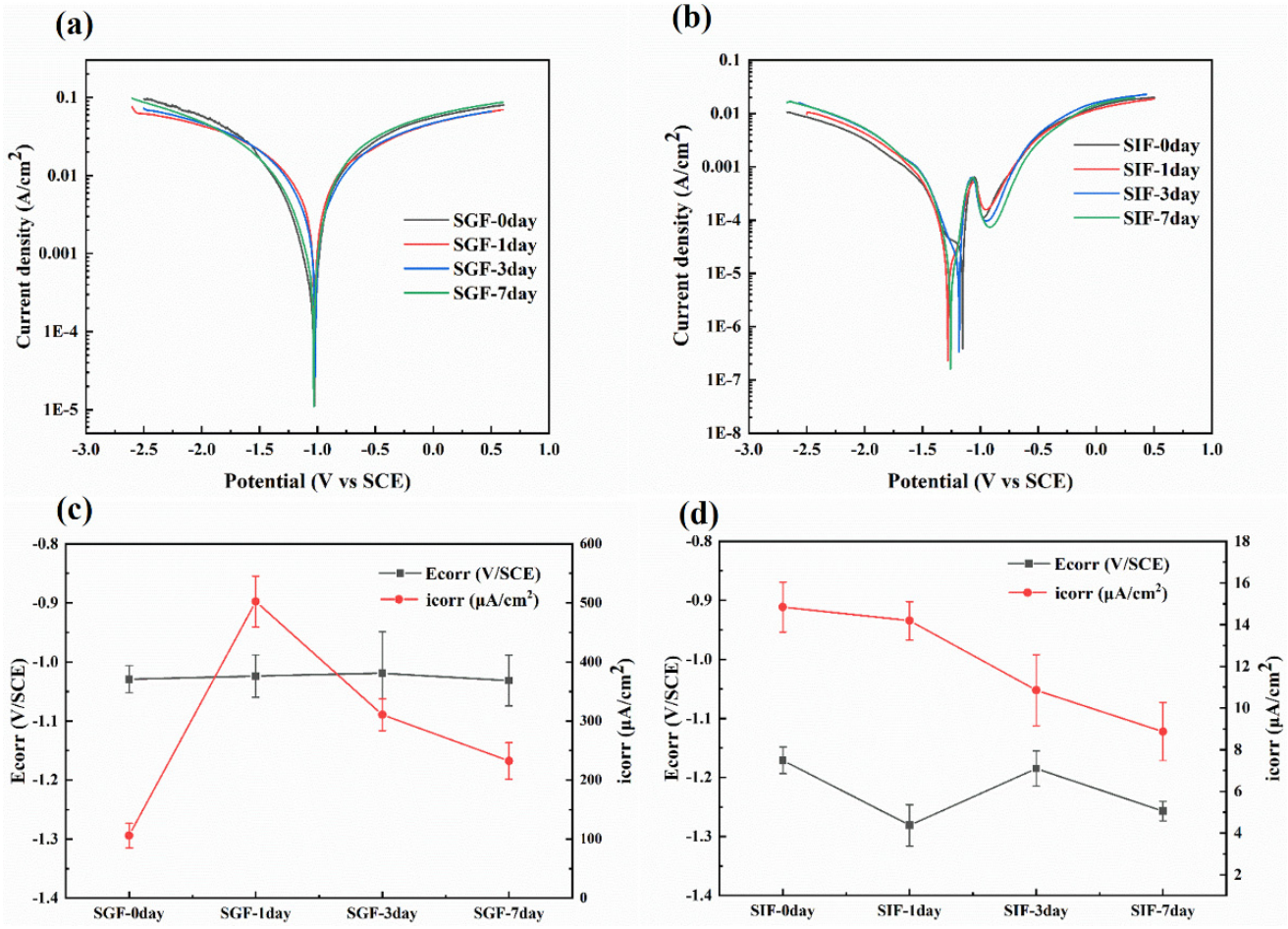

Figure 8. PDP curves of Zn–0.4Li after immersion in SGF (**a**) and SIF (**b**) for different times. Electrochemical parameters of the samples after immersion in SGF (**c**) and SIF (**d**).

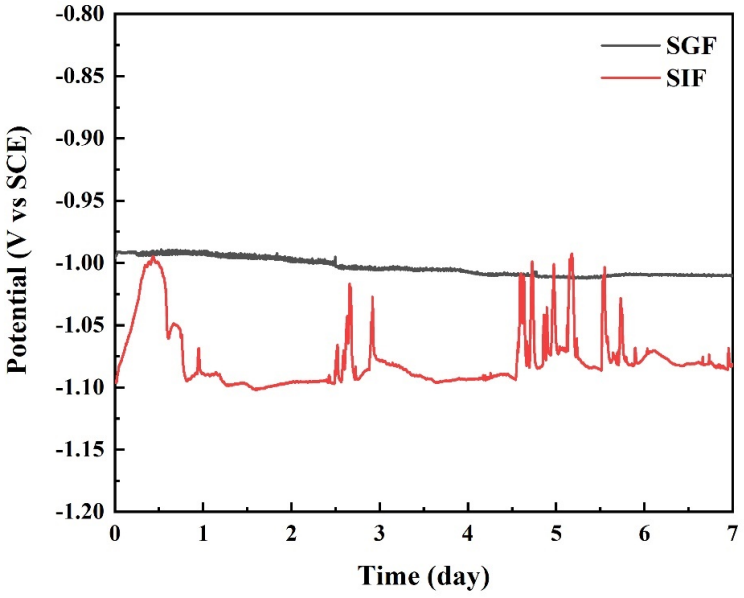

Figure 9. OCP evolution with time in the electrolytes of Zn–0.4Li immersed in SGF and SIF.

EIS is a non-destructive method for examining the reactions of corroding electrodes to small-amplitude alternating potential signals with a wide range of frequencies in order

to understand the electrochemical corrosion process in metals [59]. Figure 10 displays the comparison of EIS as Nyquist plots of Zn–0.4Li alloys measured for the samples in SGF (Figure 10a) and SIF (Figure 10b). To derive comprehensive insights into the surface reaction during immersion measurement, Bode plots were created for the impedance data (Figure 10c,d). The diameter of the capacitive loop is related to the corrosion rate; the higher the corrosion rate is, the smaller the diameter is [60,61]. The changes in the capacitance circuit diameters of the samples immersed for 1, 3 and 7 days corresponded exactly to the corrosion rate trend of SGF in Figure 2a. As can be seen in the insert in Figure 10a, the values of impedance modulus |Z| shrank within the first day and gradually increased. As is common knowledge in the oxidation community, the majority of metals can instantly produce a very thin oxidation layer when they come into contact with the air [61]. Before the fresh alloy substrate was immersed in SGF, it was quite possible that the natural oxide formed as a result of the substrate's spontaneous oxidation. On the first day, natural oxide was removed from the surface by the extremely low pH of the solution. With the gradual consumption of H^+, the product layer formed and thickened gradually (Figure 6a,c). This phenomenon also explains why i_{corr} increased on the first day of immersion, then decreased afterwards (Figure 8c).

According to the Nyquist plots (Figure 10a), one capacitive loop was evident for the sample in SGF in all intervals. One overlapped time constant was identified from the Bode plots (Figure 10c). The experimental EIS data of Zn-0.4Li immersed in SGF for 0, 1, 3, and 7 days were fitted utilizing the one-time constant model. In Figure 10, the solution resistance is denoted by R_s, and the film resistance and capacity, respectively, are denoted by R_f and CPE_f, which define the first capacity loop at medium frequency. R_{ct} and CPE_{dl}, which respectively stand for charge transfer resistance and the electric double layer at the metal/electrolyte interface, characterize the second capacity loop at low frequency. CPE is a constant phase element to compensate for the non-homogeneity in the system [62]. The CPE's electrical impedance is defined as follows [63]:

$$Z_{CPE} = \frac{1}{(j\omega)^n Y_o} \ , \tag{2}$$

where Y_o denotes the general admittance function, ω stands for the angular frequency, and the exponent n denotes a coefficient relating to the departure from pure capacitance. Table 2 contains a list of the fitting parameters. The chi-square values (χ^2) were less than 1.6×10^{-3}, indicating a satisfactory fit between the measured and simulated values.

In Figure 10f,g, the equivalent circuit models that were employed to match the SIF curves are depicted. After immersion for 0, 1, 3 and 7 days, the Nyquist curves of the samples in SIF exhibited two capacitive loops. The charge transfer resistance of the electric double layer produced the capacitive semicircle at the high frequency. It appeared in the linear zone at the low frequencies and was associated with diffusion impedance. They were adapted using the equivalent circuit with Warburg impedance [40,58,64]. Table 3 displays the corresponding parameters. The value of CPE_f decreased gradually, indicating that the corrosion product layer thickened [65]. In the EIS measurements, polarization resistance R_p was obtained by combining R_{ct} and R_f [66]. The R_p values in SIF increased with immersion time, indicating that the corrosion of Zn–0.4Li weakened with time. This result is in line with the PDP curves (Figure 8b,d).

Table 2. Fitting data of EIS for Zn–0.4Li after immersion in SGF for different times.

Solution	Immersion Time (day)	CPE_f ($10^{-4}\Omega^{-1}cm^{-2}s^{n1}$)	n1	R_f (Ωcm^2)	χ^2 (10^{-3})
SGF	0	0.67 ± 0.08	0.91 ± 0.02	37.5 ± 3.55	1.610 ± 0.108
	1	3.51 ± 0.32	0.82 ± 0.04	8.62 ± 0.89	0.233 ± 0.021
	3	2.95 ± 0.19	0.85 ± 0.05	13.3 ± 1.01	0.122 ± 0.011
	7	1.72 ± 0.07	0.87 ± 0.02	16.1 ± 1.98	0.614 ± 0.037

Table 3. Fitting data of EIS for Zn–0.4Li after immersion in SIF for different times.

Solution	Immersion Time (day)	CPE_f ($10^{-4}\Omega^{-1}cm^{-2}s^{n1}$)	n1	R_f (Ωcm^2)	CPE_{dl} ($10^{-4}\Omega^{-1}cm^{-2}$ s^{n2})	n2	R_{ct} ($k\Omega$ cm^2)	W ($10^{-4}\Omega^{-1}cm^{-2}s^{0.5}$)	χ^2 (10^{-3})
SIF	0	6.39 ± 0.52	0.70 ± 0.10	6177 ± 354	5.83 ± 1.44	0.73 ± 0.08	8.97 ± 0.65	-	0.40 ± 0.018
	1	0.50 ± 0.09	0.69 ± 0.06	175 ± 21.8	4.87 ± 0.20	0.73 ± 0.11	9.15 ± 0.87	2.78 ± 0.12	0.30 ± 0.022
	3	0.360 ± 0.05	0.73 ± 0.05	339 ± 30.4	2.05 ± 0.13	0.68 ± 0.07	9.28 ± 0.44	2.74 ± 0.23	0.44 ± 0.015
	7	0.168 ± 0.01	0.8 ± 0.09	6755 ± 467	1.29 ± 0.41	0.63 ± 0.04	16.5 ± 0.71	0.265 ± 0.04	0.85 ± 0.031

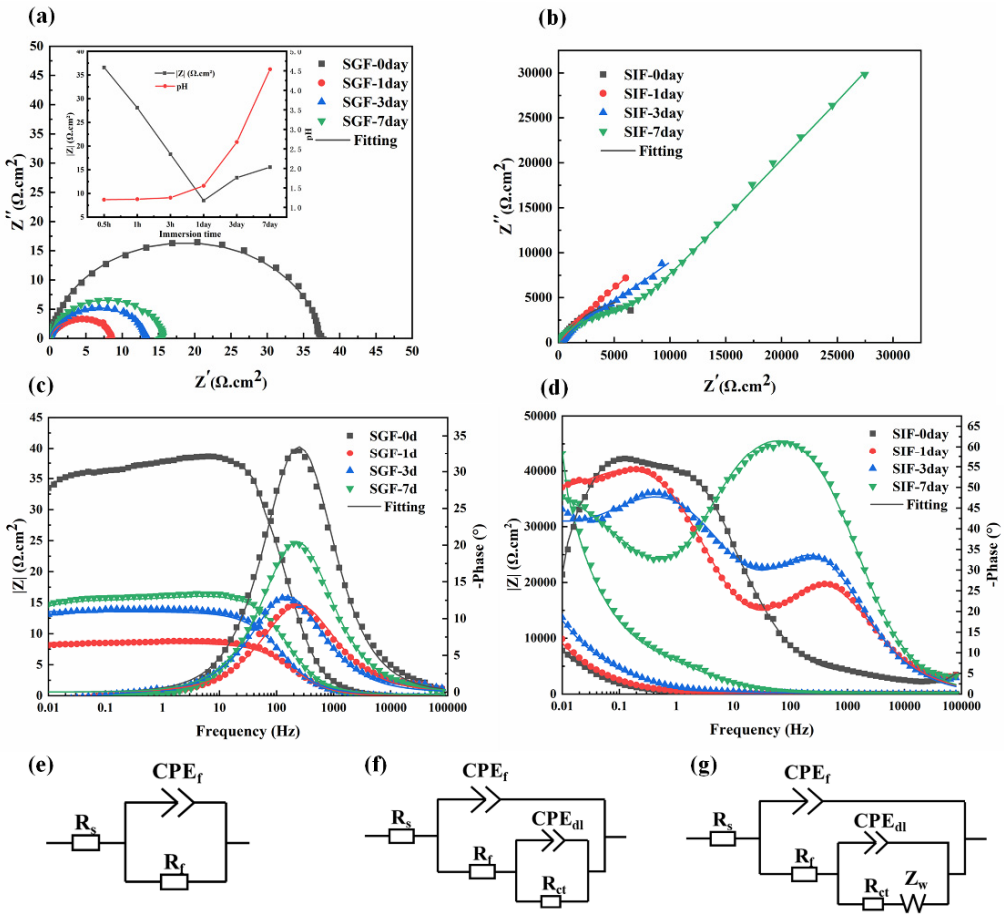

Figure 10. EIS of Zn–0.4Li immersed for different times: (**a**,**b**) Nyquist plots and (**c**,**d**) Bode plots. (**a**,**c**) For SGF, (**b**,**d**) for SIF. Diagrams (**e**–**g**) show the equivalent circuits used for EIS data. Circuit (**e**) was used to fit the EIS data obtained in SGF at all intervals, and (**f**) was used to fit the EIS data obtained in SIF on day 0 and (**g**) for 1, 3, 7 days. The insert shows the change in the values of |Z| and pH along with immersion time in (**a**).

4. Discussion

This work studied the influence of the gastrointestinal environment on the degradation behavior of Zn–0.4Li alloys by using simulated gastric and intestinal fluids. Similarly to albumin, pepsin and pancreatin are proteins made of many amino acids connected by peptide bonds. The Langmuir adsorption isotherm has been utilized to describe the adsorption of albumin onto metal surfaces [67]. The value of Gibbs free energy of adsorption obtained from the Langmuir adsorption isotherm can reveal whether albumin molecules are adsorbed on pure Zn surfaces through chemisorption or physisorption [40]. However, no adsorption isotherm can be used for pepsin and pancreatin. The proteins are commonly perceived to have a chelating and barrier function. Delayed corrosion was confirmed due to the physical barrier created by proteins adhering to the metal surface [40,68–70]. The GD-OES and XPS spectra in the current study indicated the existence of organic components in the corrosion layer. Both enzymes affected the formation of the degradation products.

Specifically, Li^+ was released prior to Zn^{2+} during immersion in SGF and SIF from the releasement of the Li^+/Zn^{2+} atomic ratio in Figure 7. The first reason is that the Li atom in the corrosion layer exhibits superior mobility and activity and readily combines with the aqueous environment to generate Li-containing compounds in the external corrosion layer [71]. The second reason is that the E° of Li (i.e., −3.04 V) is much lower than that of Zn (i.e., −0.76 V) [27]. The corrosion mechanisms of Zn–0.4Li immersed in SGF and SIF are shown in Figure 11.

For the samples immersed in SGF, the near-surface area of the sample was divided into Li-rich and matrix regions (Figure 6a). At the interface 1 of direct contact between matrix and solution (Figure 10a), Li reacted first and released an amount of Li^+ ions, alkaline hydroxyl anions and hydrogen gas (Formulas (3) and (4)).

$$Li(s) \rightarrow Li^+(aq) + e^- \quad (3)$$

$$2H_2O + 2e^- \rightarrow H_2(g)\uparrow + 2OH^-(aq) \quad (4)$$

$$2Li^+ + CO_3^{2-} \rightarrow Li_2CO_3(s) \quad (5)$$

The released Li^+ ions could react with CO_3^{2-} ions in the SGF according to Formula (5) to form Li_2CO_3. The Li_2CO_3 nuclei grew continuously, and Li-rich products thickened because there were adequate Li^+ and CO_3^{2-} ions available.

Subsequently, after the near-surface region became Li-poor, the reaction between Zn and H_2O at the interface 2 became dominant and resulted in the formation of $Zn(OH)_2$, parts of which were likely to be dehydrated to form ZnO [72] or react with the dissolved CO_2 in SGF to form $Zn_5(CO_3)_2(OH)_6$ [73].

According to XRD and XPS (Figures 3c and 5a), the corrosion products were formed according to the following reactions:

$$Zn + 2H_2O \rightarrow H_2(g)\uparrow + Zn(OH)_2(s) \quad (6)$$

$$Zn(OH)_2(s) \rightarrow ZnO(s) + H_2O \quad (7)$$

$$Zn(OH)_2(s) + 4Zn^{2+} + 4OH^- + 2CO_3^{2-} \rightarrow Zn_5(CO_3)_2(OH)_6(s) \quad (8)$$

During the initial immersion in SGF (Figure 10a), hydrogen evolution and adsorption of enzymes occurred simultaneously. From XPS and GD-OES (Figures 5 and 6), pepsin contributed to the development of corrosion products and mainly existed in the Zn-rich product region. The surface became uneven due to the combined effect of chlorine and hydrogen ions, and severe localized corrosion occurred, then extended further (Figure 3a). Additionally, the surface of the sample was covered with a layer of loose corrosion products. The adsorption of pepsin and the corrosion layer could not alleviate the Cl^- attack in SGF due to the extremely low pH of the solution, resulting in the diminution of the $|Z|$ value (Figure 10a). A Li-poor region of the substrate could be discovered below the corrosion layer as a result of the deeper substrate's Li atoms being unable to diffuse to the surface in a timely manner (Figure 6). With the increase in immersion time, the Li-rich region migrated to the interior of the sample, and the range was enlarged. The weight percentage of the element N in the dissolved region of the sample surface decreased from 0.733 to 0.309 (Figure 6a,c), indicating that the amount of the enzyme adsorbed on the sample surface decreased, possibly due to enzyme shedding or hydrolysis during the immersion process (Figure 11a). However, because of the accumulation of the corrosion products, the corrosion product layer increased the film resistance, and the corrosion resistance of the samples was improved, as demonstrated by the corrosion rate, polarization curve and impedance spectrum (Figures 2a, 8c and 10a).

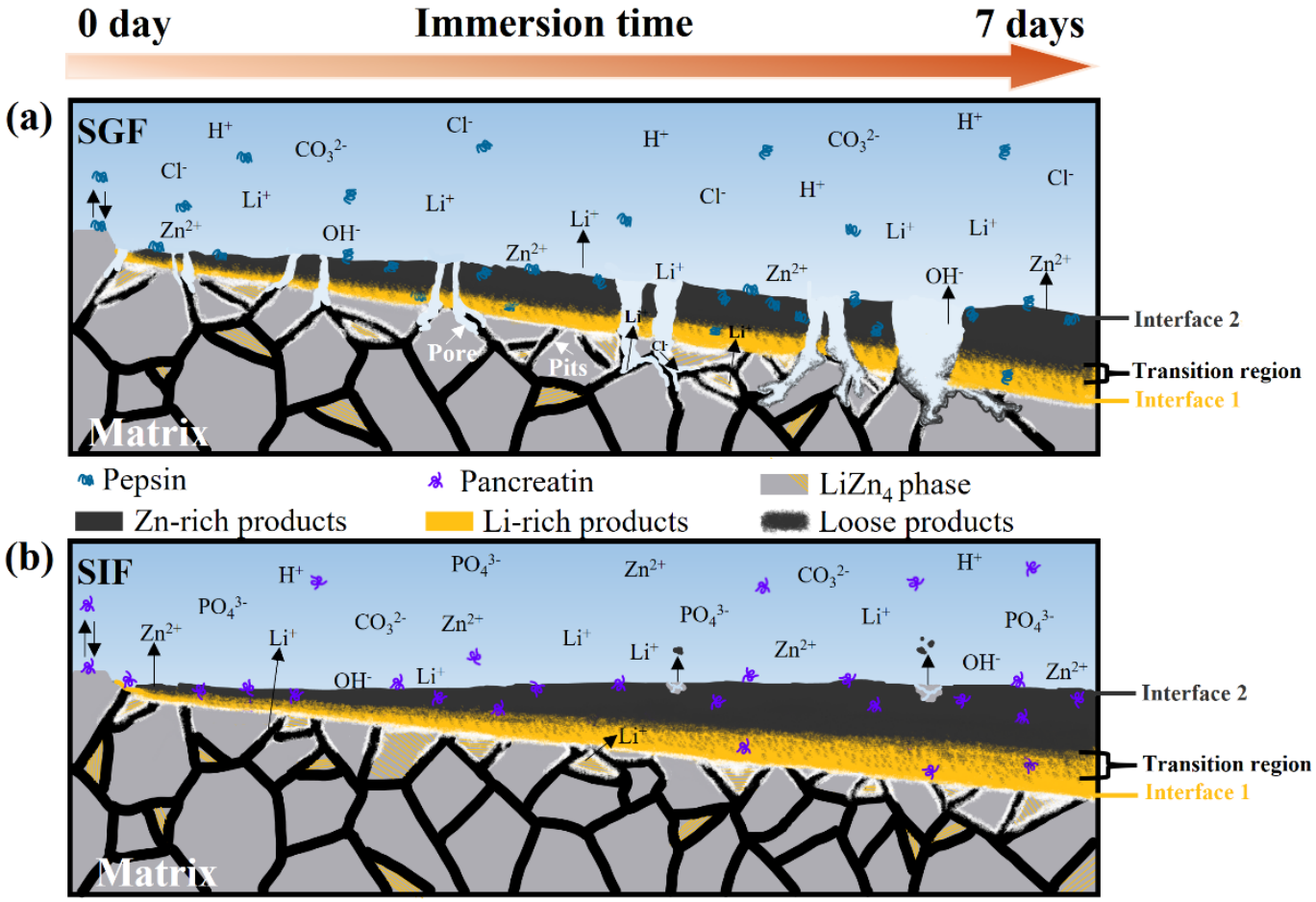

Figure 11. Schematic illustration of Zn–0.4Li alloy degradation in different solutions as the immersion time increases. (**a**) Degradation in SGF and (**b**) degradation in SIF.

For SIF, the dissolution of Zn–0.4Li and the formation of Zn phosphate are presented in Figures 3c and 5(a1). Notably, the deposition of phosphate helps decrease the corrosion rate and uniform corrosion of metals [52,74,75]. According to the SEM images, the samples were uniformly corroded (Figure 3b). Although the adsorbed pancreatin was implicated in the production of the corrosion products, it was less dense than the Zn phosphate layer, which allowed the aqueous solution to penetrate it easily [70]. As a result, Li-poor regions and a Li-rich region can be observed in Figure 6b,d. With the accumulation of phosphates, the charge transfer at the interfaces was hindered. Hence, the corrosion resistance of Zn–0.4Li improved. The corrosion mechanism of the Li-rich and Li-poor regions close to the sample surface area was similar to that of SGF when samples were immersed in SIF. During immersion in SIF (Figure 11b), the reaction type of Zn and H_2O at interface 2 differed from that in SGF. Dissolution of Zn takes place in accordance with Equations (8) and (9):

$$Zn \rightarrow Zn^{2+} + 2e^{-} \quad (9)$$

$$O_2 + 2H_2O + 4e^{-} \rightarrow 4OH^{-} \quad (10)$$

In the Zn-rich region of the sample in SIF, Zn and the ions in the solution formed Zn carbonate and Zn phosphate. The OCP of SIF changed periodically within a period of about 2.5 days (Figure 9). The phenomenon may have resulted from the adsorption and subsequent desorption of pancreatin or the shedding of corrosion products during immersion (Figure 11b). The Zn-rich and Li-rich regions of the samples immersed in SIF were always thicker than those of the samples immersed in SGF (Figure 11).

5. Conclusions

In the present study, the influence of the gastrointestinal environment on the corrosion of Zn alloys was investigated.

1. In SGF, the samples were severely corroded locally, and the corrosion pits had a maximum diameter of over 150 μm. In SIF, the samples were uniformly corroded.
2. The generation of the degradation product layer involved the digestive enzymes pepsin and pancreatin. The amount of enzyme attached to the surface of the sample decreased with immersion time because of solution flushing or hydrolysis of enzymes. The adsorption and subsequent desorption of pancreatin or the shedding of corrosion products occurred when the specimens were immersed in SIF.
3. Following immersion in SGF and SIF, Li-poor and Li-rich regions were observed in the near-surface of the samples. In the surface of samples where direct contact with the solution occurred, Li reacted first and released an amount of Li^+ ions. Then Li^+ ions reacted dominantly with CO_3^{2-} to form significant amounts of Li_2CO_3 to form the Li-rich region. Due to that, Li atoms in the deeper part of the matrix could not diffuse to the surface in time, and the Li-poor region of the substrate beneath the Li-rich region was formed. When Li was depleted, the reaction between Zn and H_2O became dominant and formed Zn-rich products with time. The extent of the Li-rich region increased with immersion time because of the accumulation of the corrosion products.
4. Li^+ releasement dominated over Zn^{2+} releasement throughout the immersion process in SGF and SIF.

Author Contributions: M.W.: Investigation, Methodology, Data curation, Writing—original draft. L.Y. (Lingbo Yang): Data curation. X.Z.: Investigation. L.Y. (Lijing Yang): Writing—review and editing, Funding acquisition, Supervision. J.S., T.L.: Conceptualization. Z.S., H.L.: Conceptualization, Resources, Supervision. All authors have read and agreed to the published version of the manuscript.

Funding: This work was supported by National key research and development program (2019YFE0118600).

Institutional Review Board Statement: Not applicable.

Informed Consent Statement: Not applicable.

Data Availability Statement: The raw/processed data required to reproduce these findings cannot be shared at this time as the data also form part of an ongoing study.

Conflicts of Interest: The authors declare no conflict of interest.

References

1. Du, W.B.; Liu, K.; Ma, K.; Wang, Z.H.; Li, S.B. Effects of trace Ca/Sn addition on corrosion behaviors of biodegradable Mg-4Zn-0.2Mn alloy. *J. Magnes. Alloy.* **2018**, *6*, 1–14. [CrossRef]
2. Yan, J.; Chen, Y.; Yuan, Q.; Wang, X.; Yu, S.; Qiu, W.; Wang, Z.; Ai, K.; Zhang, X.; Zhang, S.; et al. Comparison of the effects of Mg-6Zn and Ti-3Al-2.5V alloys on TGF-beta/TNF-alpha/VEGF/b-FGF in the healing of the intestinal tract in vivo. *Biomed. Mater.* **2014**, *9*, 025011. [CrossRef]
3. Yan, J.; Chen, Y.; Yuan, Q.; Yu, S.; Qiu, W.; Yang, C.; Wang, Z.; Gong, J.; Ai, K.; Zheng, Q.; et al. Comparison of the effects of Mg-6Zn and titanium on intestinal tract in vivo. *J. Mater. Sci.-Mater. Med.* **2013**, *24*, 1515–1525. [CrossRef]
4. Yang, H.T.; Jia, B.; Zhang, Z.C.; Qu, X.H.; Li, G.N.; Lin, W.J.; Zhu, D.H.; Dai, K.R.; Zheng, Y.F. Alloying design of biodegradable zinc as promising bone implants for load-bearing applications. *Nat. Commun.* **2020**, *11*, 401. [CrossRef] [PubMed]
5. Yang, H.T.; Qu, X.H.; Wang, M.Q.; Cheng, H.W.; Jia, B.; Nie, J.F.; Dai, K.R.; Zheng, Y.F. Zn-0.4Li alloy shows great potential for the fixation and healing of bone fractures at load-bearing sites. *Chem. Eng. J.* **2021**, *417*, 12. [CrossRef]
6. Guo, P.S.; Zhu, X.L.; Yang, L.J.; Deng, L.; Zhang, Q.K.; Li, B.Q.; Cho, K.; Sun, W.S.; Ren, T.T.; Song, Z.L. Ultrafine- and uniform-grained biodegradable Zn-0.5Mn alloy: Grain refinement mechanism, corrosion behavior, and biocompatibility in vivo. *Mat. Sci. Eng. C-Mater.* **2021**, *118*, 111391. [CrossRef] [PubMed]
7. Yang, L.J.; Guo, P.S.; Niu, Z.G.; Li, F.X.; Song, Z.L.; Xu, C.; Liu, H.N.; Sun, W.S.; Ren, T.T. Influence of Mg on the mechanical properties and degradation performance of as-extruded Zn-Mg-Ca alloys: In vitro and in vivo behavior. *J. Mech. Behav. Biomed. Mater.* **2019**, *95*, 220–231. [CrossRef] [PubMed]

8. Shi, Y.X.; Yang, L.J.; Wang, L.C.; Zhang, Q.K.; Zhu, X.L.; Sun, W.S.; Shen, J.W.; Lu, T.; Song, Z.L.; Liu, H.N. Corrosion and Biocompatibility of Pure Zn with a Micro-Arc-Oxidized Layer Coated with Calcium Phosphate. *Coatings* **2021**, *11*, 1425. [CrossRef]
9. Guo, H.; He, Y.; Zheng, Y.F.; Cui, Y. In vitro studies of biodegradable Zn-0.1Li alloy for potential esophageal stent application. *Mater. Lett.* **2020**, *275*, 4. [CrossRef]
10. Jia, B.; Yang, H.T.; Han, Y.; Zhang, Z.C.; Qu, X.H.; Zhuang, Y.F.; Wu, Q.; Zheng, Y.F.; Dai, K.R. In vitro and in vivo studies of Zn-Mn biodegradable metals designed for orthopedic applications. *Acta Biomater.* **2020**, *108*, 358–372. [CrossRef]
11. Sun, J.; Zhang, X.; Shi, Z.Z.; Gao, X.X.; Li, H.Y.; Zhao, F.Y.; Wang, J.Q.; Wang, L.N. Development of a high-strength Zn-Mn-Mg alloy for ligament reconstruction fixation. *Acta Biomater.* **2021**, *119*, 485–498. [CrossRef] [PubMed]
12. Yuan, W.; Xia, D.D.; Zheng, Y.F.; Liu, X.M.; Wu, S.L.; Li, B.; Han, Y.; Jia, Z.J.; Zhu, D.H.; Ruan, L.Q.; et al. Controllable biodegradation and enhanced osseointegration of ZrO2-nanofilm coated Zn-Li alloy: In vitro and in vivo studies. *Acta Biomater.* **2020**, *105*, 290–303. [CrossRef]
13. Bordbar-Khiabani, A.; Ebrahimi, S.; Yarmand, B. In-vitro corrosion and bioactivity behavior of tailored calcium phosphate-containing zinc oxide coating prepared by plasma electrolytic oxidation. *Corros. Sci.* **2020**, *173*. [CrossRef]
14. Guo, H.; Hu, J.L.; Shen, Z.Q.; Du, D.X.; Zheng, Y.F.; Peng, J.R. In vitro and in vivo studies of biodegradable Zn-Li-Mn alloy staples designed for gastrointestinal anastomosis. *Acta Biomater.* **2021**, *121*, 713–723. [CrossRef] [PubMed]
15. Fallingborg, J. Intraluminal pH of the human gastrointestinal tract. *Dan. Med. Bull.* **1999**, *46*, 183–196. [PubMed]
16. Vertzoni, M.; Pastelli, E.; Psachoulias, D.; Kalantzi, L.; Reppas, C. Estimation of intragastric solubility of drugs: In what medium? *Pharm. Res.* **2007**, *24*, 909–917. [CrossRef] [PubMed]
17. Falavigna, M.; Klitgaard, M.; Steene, E.; Flaten, G.E. Mimicking regional and fasted/fed state conditions in the intestine with the mucus-PVPA in vitro model: The impact of pH and simulated intestinal fluids on drug permeability. *Eur. J. Pharm. Sci.* **2019**, *132*, 44–54. [CrossRef]
18. Bowen, P.K.; Drelich, J.; Goldman, J. Zinc Exhibits Ideal Physiological Corrosion Behavior for Bioabsorbable Stents. *Adv. Mater.* **2013**, *25*, 2577–2582. [CrossRef]
19. Shi, Z.Z.; Yu, J.; Liu, X.F. Microalloyed Zn-Mn alloys: From extremely brittle to extraordinarily ductile at room temperature. *Mater. Des.* **2018**, *144*, 343–352. [CrossRef]
20. Sikora-Jasinska, M.; Mostaed, E.; Mostaed, A.; Beanland, R.; Mantovani, D.; Vedani, M. Fabrication, mechanical properties and in vitro degradation behavior of newly developed Zn-Ag alloys for degradable implant applications. *Mat. Sci. Eng. C-Mater.* **2017**, *77*, 1170–1181. [CrossRef]
21. Zhao, S.; McNamara, C.T.; Bowen, P.K.; Verhun, N.; Braykovich, J.P.; Goldman, J.; Drelich, J.W. Structural Characteristics and In Vitro Biodegradation of a Novel Zn-Li Alloy Prepared by Induction Melting and Hot Rolling. *Met. Mater. Trans. A-Phys. Metall. Mater. Sci.* **2017**, *48A*, 1204–1215. [CrossRef]
22. Dai, Y.L.; Zhang, Y.; Liu, H.; Fang, H.J.; Li, D.; Xu, X.M.; Yan, Y.; Chen, L.J.; Lu, Y.J.; Yu, K. Mechanical strengthening mechanism of Zn-Li alloy and its mini tube as potential absorbable stent material. *Mater. Lett.* **2019**, *235*, 220–223. [CrossRef]
23. Jin, H.L.; Zhao, S.; Guillory, R.; Bowen, P.K.; Yin, Z.Y.; Griebel, A.; Schaffer, J.; Earley, E.J.; Goldman, J.; Drelich, J.W. Novel high-strength, low-alloys Zn-Mg (<0.1 wt% Mg) and their arterial biodegradation. *Mat. Sci. Eng. C-Mater.* **2018**, *84*, 67–79. [CrossRef]
24. Mostaed, E.; Sikora-Jasinska, M.; Mostaed, A.; Loffredo, S.; Demir, A.G.; Preuitali, B.; Mantouani, D.; Beanland, R.; Vedani, M. Novel Zn-based alloys for biodegradable stent applications: Design, development and in vitro degradation. *J. Mech. Behav. Biomed. Mater.* **2016**, *60*, 581–602. [CrossRef]
25. Tong, X.; Zhang, D.C.; Zhang, X.T.; Su, Y.C.; Shi, Z.M.; Wang, K.; Lin, J.G.; Li, Y.C.; Lin, J.X.; Wen, C. Microstructure, mechanical properties, biocompatibility, and in vitro corrosion and degradation behavior of a new Zn-5Ge alloy for biodegradable implant materials. *Acta Biomater.* **2018**, *82*, 197–204. [CrossRef] [PubMed]
26. Shen, C.; Liu, X.W.; Fan, B.; Lan, P.H.; Zhou, F.Y.; Li, X.K.; Wang, H.L.; Xiao, X.; Li, L.; Zhao, S.; et al. Mechanical properties, in vitro degradation behavior, hemocompatibility and cytotoxicity evaluation of Zn-1.2Mg alloy for biodegradable implants. *RSC Adv.* **2016**, *6*, 86410–86419. [CrossRef]
27. Li, Z.; Shi, Z.Z.; Hao, Y.; Li, H.F.; Liu, X.F.; Volinsky, A.A.; Zhang, H.J.; Wang, L.N. High-performance hot-warm rolled Zn-0.8Li alloy with nano-sized metastable precipitates and sub-micron grains for biodegradable stents. *J. Mater. Sci. Technol.* **2019**, *35*, 2618–2624. [CrossRef]
28. Zhao, S.; Seitz, J.M.; Eifler, R.; Maier, H.J.; Guillory, R.J.; Earley, E.J.; Drelich, A.; Goldman, J.; Drelich, J.W. Zn-Li alloy after extrusion and drawing: Structural, mechanical characterization, and biodegradation in abdominal aorta of rat. *Mater. Sci. Eng. C-Mater. Biol. Appl.* **2017**, *76*, 301–312. [CrossRef]
29. Wang, Z.; Zhang, Q.K.; Bagheri, R.; Guo, P.S.; Yao, Y.R.; Yang, L.J.; Song, Z.L. Influence of laser surface remelting on microstructure and degradation mechanism in simulated body fluid of Zn-0.5Zr alloy. *J. Mater. Sci. Technol.* **2019**, *35*, 2705–2713. [CrossRef]
30. Aral, H.; Vecchio-Sadus, A. Toxicity of lithium to humans and the environment—A literature review. *Ecotoxicol. Environ. Saf.* **2008**, *70*, 349–356. [CrossRef] [PubMed]
31. Chen, P.H.; Hsiao, C.Y.; Chiang, S.J.; Shen, R.S.; Lin, Y.K.; Chung, K.H.; Tsai, S.Y. Cardioprotective potential of lithium and role of fractalkine in euthymic patients with bipolar disorder. *Aust. N. Zeal. J. Psychiatry* **2021**, *57*, 104–114. [CrossRef]
32. Mazor, M.; Kawano, Y.; Zhu, H.N.; Waxman, J.; Kypta, R.M. Inhibition of glycogen synthase kinase-3 represses androgen receptor activity and prostate cancer cell growth. *Oncogene* **2004**, *23*, 7882–7892. [CrossRef] [PubMed]

33. Young, W. Review of Lithium Effects on Brain and Blood. *Cell Transplant.* **2009**, *18*, 951–975. [CrossRef] [PubMed]
34. Witte, F.; Hort, N.; Vogt, C.; Cohen, S.; Kainer, K.U.; Willumeit, R.; Feyerabend, F. Degradable biomaterials based on magnesium corrosion. *Curr. Opin. Solid State Mater. Sci.* **2008**, *12*, 63–72. [CrossRef]
35. Hernandez-Escobar, D.; Champagne, S.; Yilmazer, H.; Dikici, B.; Boehlert, C.J.; Hermawan, H. Current status and perspectives of zinc-based absorbable alloys for biomedical applications. *Acta Biomater.* **2019**, *97*, 1–22. [CrossRef]
36. Zhang, S.X.; Zhang, X.N.; Zhao, C.L.; Li, J.A.; Song, Y.; Xie, C.Y.; Tao, H.R.; Zhang, Y.; He, Y.H.; Jiang, Y.; et al. Research on an Mg-Zn alloy as a degradable biomaterial. *Acta Biomater.* **2010**, *6*, 626–640. [CrossRef] [PubMed]
37. Pelton, A.D. The Li-Zn (Lithium-Zinc) System. *J. Phase Equilibria* **1991**, *12*, 42–45. [CrossRef]
38. Li, Z.; Shi, Z.Z.; Zhang, H.J.; Li, H.F.; Feng, Y.; Wang, L.N. Hierarchical microstructure and two-stage corrosion behavior of a high-performance near-eutectic Zn-Li alloy. *J. Mater. Sci. Technol.* **2021**, *80*, 50–65. [CrossRef]
39. Li, Z.; Shi, Z.Z.; Hao, Y.; Li, H.F.; Zhang, H.J.; Liu, X.F.; Wang, L.N. Insight into role and mechanism of Li on the key aspects of biodegradable Zn-Li alloys: Microstructure evolution, mechanical properties, corrosion behavior and cytotoxicity. *Mater. Sci. Eng. C-Mater. Biol. Appl.* **2020**, *114*, 111049. [CrossRef]
40. Liu, L.J.; Lu, L.L.; Zhang, H.J.; Wang, L.N. Influence of bovine serum albumin on corrosion behaviour of pure Zn in phosphate buffered saline. *J. Mater. Sci.-Mater. Med.* **2021**, *32*, 95. [CrossRef]
41. Song, Y.W.; Shan, D.Y.; Chen, R.S.; Han, E.H. Corrosion characterization of Mg-8Li alloy in NaCl solution. *Corros. Sci.* **2009**, *51*, 1087–1094. [CrossRef]
42. Duchoslav, J.; Steinberger, R.; Arndt, M.; Stifter, D. XPS study of zinc hydroxide as a potential corrosion product of zinc: Rapid X-ray induced conversion into zinc oxide. *Corros. Sci.* **2014**, *82*, 356–361. [CrossRef]
43. Li, Z.; Shi, Z.Z.; Yan, Y.; Zhang, D.W.; Yang, K.; Li, H.F.; Zhang, H.J.; Wang, L.N. Suppression mechanism of initial pitting corrosion of pure Zn by Li alloying. *Corros. Sci.* **2021**, *189*, 109564. [CrossRef]
44. Bautista, B.E.T.; Carvalho, M.L.; Seyeux, A.; Zanna, S.; Cristiani, P.; Tribollet, B.; Marcus, P.; Frateur, I. Effect of protein adsorption on the corrosion behavior of 70Cu-30Ni alloy in artificial seawater. *Bioelectrochemistry* **2014**, *97*, 34–42. [CrossRef] [PubMed]
45. Lee, H.H.; Bae, M.; Jo, S.H.; Shin, J.K.; Son, D.H.; Won, C.H.; Lee, J.H. Differential-mode HEMT-based biosensor for real-time and label-free detection of C-reactive protein. *Sens. Actuators B-Chem.* **2016**, *234*, 316–323. [CrossRef]
46. Vanea, E.; Simon, V. XPS study of protein adsorption onto nanocrystalline aluminosilicate microparticles. *Appl. Surf. Sci.* **2011**, *257*, 2346–2352. [CrossRef]
47. Wan, P.; Lin, X.; Tan, L.L.; Li, L.G.; Li, W.R.; Yang, K. Influence of albumin and inorganic ions on electrochemical corrosion behavior of plasma electrolytic oxidation coated magnesium for surgical implants. *Appl. Surf. Sci.* **2013**, *282*, 186–194. [CrossRef]
48. Wang, M.L.; Yang, L.B.; Zhu, X.L.; Yang, L.J.; Song, Z.L. Influence of Enzymes on the In Vitro Degradation Behavior of Pure Zn in Simulated Gastric and Intestinal Fluids. *ACS Omega* **2022**, *8*, 1331–1342. [CrossRef]
49. Dong, H.Z.; Lin, F.; Boccaccini, A.R.; Virtanen, S. Corrosion behavior of biodegradable metals in two different simulated physiological solutions: Comparison of Mg, Zn and Fe. *Corros. Sci.* **2021**, *182*, 109278. [CrossRef]
50. Yan, Y.; Zhou, P.; Gharbi, O.; Zeng, Z.; Chen, X.; Volovitch, P.; Ogle, K.; Birbilis, N. Investigating ion release using inline ICP during in situ scratch testing of an Mg-Li(-Al-Y-Zr) alloy. *Electrochem. Commun.* **2019**, *99*, 46–50. [CrossRef]
51. Zhao, M.C.; Liu, M.; Song, G.L.; Atrens, A. Influence of pH and chloride ion concentration on the corrosion of Mg alloy ZE41. *Corros. Sci.* **2008**, *50*, 3168–3178. [CrossRef]
52. Jang, Y.; Collins, B.; Sankar, J.; Yun, Y. Effect of biologically relevant ions on the corrosion products formed on alloy AZ31B: An improved understanding of magnesium corrosion. *Acta Biomater.* **2013**, *9*, 8761–8770. [CrossRef] [PubMed]
53. Munoz, A.I.; Mischler, S. Interactive effects of albumin and phosphate ions on the corrosion of CoCrMo implant alloy. *J. Electrochem. Soc.* **2007**, *154*, C562–C570. [CrossRef]
54. Zhang, Y.; Cao, J.; Wang, X.L.; Liu, H.; Shao, Y.; Chu, C.L.; Xue, F.; Bai, J. The effect of enzymes on the in vitro degradation behavior of Mg alloy wires in simulated gastric fluid and intestinal fluid. *Bioact. Mater.* **2022**, *7*, 217–226. [CrossRef] [PubMed]
55. Medhashree, H.; Shetty, A.N. Electrochemical corrosion study of Mg-Al-Zn-Mn alloy in aqueous ethylene glycol containing chloride ions. *J. Mater. Res. Technol.-JMRT* **2017**, *6*, 40–49. [CrossRef]
56. Jamesh, M.I.; Wu, G.; Zhao, Y.; McKenzie, D.R.; Bilek, M.M.M.; Chu, P.K. Electrochemical corrosion behavior of biodegradable Mg-Y-RE and Mg-Zn-Zr alloys in Ringer's solution and simulated body fluid. *Corros. Sci.* **2015**, *91*, 160–184. [CrossRef]
57. McCafferty, E. Validation of corrosion rates measured by the Tafel extrapolation method. *Corros. Sci.* **2005**, *47*, 3202–3215. [CrossRef]
58. Liu, L.; Meng, Y.; Volinsky, A.A.; Zhang, H.-J.; Wang, L.-N. Influences of albumin on in vitro corrosion of pure Zn in artificial plasma. *Corros. Sci.* **2019**, *153*, 341–356. [CrossRef]
59. Perez, N. *Electrochemistry and Corrosion Science*, 1st ed.; Springer: New York, NY, USA, 2004.
60. Rosalbino, F.; De Negri, S.; Scavino, G.; Saccone, A. Microstructure and in vitro degradation performance of Mg-Zn-Mn alloys for biomedical application. *J. Biomed. Mater. Res. Part A* **2013**, *101*, 704–711. [CrossRef] [PubMed]
61. Pouilleau, J.; Devilliers, D.; Garrido, F.; DurandVidal, S. Structure and composition of passive titanium oxide films. *Mat. Sci. Eng. B-Solid* **1997**, *47*, 235–243. [CrossRef]
62. Song, Y.W.; Han, E.H.; Shan, D.Y.; Yim, C.D.; You, B.S. The effect of Zn concentration on the corrosion behavior of Mg-xZn alloys. *Corros. Sci.* **2012**, *65*, 322–330. [CrossRef]

63. Karimi, S.; Nickchi, T.; Alfantazi, A. Effects of bovine serum albumin on the corrosion behaviour of AISI 316L, Co-28Cr-6Mo, and Ti-6Al-4V alloys in phosphate buffered saline solutions. *Corros. Sci.* **2011**, *53*, 3262–3272. [CrossRef]
64. Ye, C.T.; Jia, L.N.; Xu, G.X.; Wang, F.F.; Wang, X.C.; Zhang, H. Microstructure and initial corrosion behavior of double-layer Zn-Al-Mg coatings produced by PVD. *Surf. Coat. Technol.* **2019**, *366*, 214–226. [CrossRef]
65. Wang, C.M.; Shen, J.; Xie, F.X.; Duan, B.; Xie, X. A versatile dopamine-induced intermediate layer for polyether imides (PEI) deposition on magnesium to render robust and high inhibition performance. *Corros. Sci.* **2017**, *122*, 32–40. [CrossRef]
66. King, A.D.; Birbilis, N.; Scully, J.R. Accurate Electrochemical Measurement of Magnesium Corrosion Rates; a Combined Impedance, Mass-Loss and Hydrogen Collection Study. *Electrochim. Acta* **2014**, *121*, 394–406. [CrossRef]
67. Vidal, C.V.; Juan, A.O.; Munoz, A.L. Adsorption of bovine serum albumin on CoCrMo surface: Effect of temperature and protein concentration. *Colloid Surf. B* **2010**, *80*, 1–11. [CrossRef]
68. Zheng, Y.F.; Gu, X.N.; Witte, F. Biodegradable metals. *Mat. Sci. Eng. R* **2014**, *77*, 1–34. [CrossRef]
69. Advincula, M.; Fan, X.W.; Lemons, J.; Advincula, R. Surface modification of surface sol-gel derived titanium oxide films by self-assembled monolayers (SAMS) and non-specific protein adsorption studies. *Colloid Surf. B* **2005**, *42*, 29–43. [CrossRef]
70. Wang, Y.S.; Lim, C.S.; Lim, C.V.; Yong, M.S.; Teo, E.K.; Moh, L.N. In vitro degradation behavior of M1A magnesium alloy in protein-containing simulated body fluid. *Mat. Sci. Eng. C-Mater.* **2011**, *31*, 579–587. [CrossRef]
71. Zeng, R.C.; Sun, L.; Zheng, Y.F.; Cui, H.Z.; Han, E.H. Corrosion and characterisation of dual phase Mg-Li-Ca alloy in Hank's solution: The influence of microstructural features. *Corros. Sci.* **2014**, *79*, 69–82. [CrossRef]
72. Liu, X.; Yang, H.T.; Liu, Y.; Xiong, P.; Guo, H.; Huang, H.H.; Zheng, Y.F. Comparative Studies on Degradation Behavior of Pure Zinc in Various Simulated Body Fluids. *Jom-Us* **2019**, *71*, 1414–1425. [CrossRef]
73. Graedel, T.E. Corrosion Mechanisms for Zinc Exposed to the Atmosphere. *J. Electrochem. Soc.* **1989**, *136*, C193–C203. [CrossRef]
74. Wang, W.; Mohammadi, F.; Alfantazi, A. Corrosion behaviour of niobium in phosphate buffered saline solutions with different concentrations of bovine serum albumin. *Corros. Sci.* **2012**, *57*, 11–21. [CrossRef]
75. Zeng, R.C.; Hu, Y.; Guan, S.K.; Cui, H.Z.; Han, E.H. Corrosion of magnesium alloy AZ31: The influence of bicarbonate, sulphate, hydrogen phosphate and dihydrogen phosphate ions in saline solution. *Corros. Sci.* **2014**, *86*, 171–182. [CrossRef]

Disclaimer/Publisher's Note: The statements, opinions and data contained in all publications are solely those of the individual author(s) and contributor(s) and not of MDPI and/or the editor(s). MDPI and/or the editor(s) disclaim responsibility for any injury to people or property resulting from any ideas, methods, instructions or products referred to in the content.